UC San Diego
UC San Diego Previously Published Works

Title

The East Pacific Rise current: Topographic enhancement of the interior flow in the South Pacific Ocean

Permalink

Journal

ISSN

Authors

Zilberman, NV
Roemmich, DH
Gille, ST

Publication Date

DOI

Peer reviewed
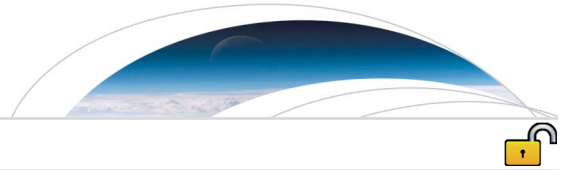
Key Points:
- A northward current is found along the western flank of the East Pacific Rise between 42°S and 30°S
- The East Pacific Rise creates a window for enhanced meridional transport of intermediate water masses and deeper waters
- About half of the East Pacific Rise current transport can be explained by topographic steering of the deep flow over the East Pacific Rise

Correspondence to:
N. V. Zilberman,
nzilberman@ucsd.edu

The East Pacific Rise current: Topographic enhancement of the interior flow in the South Pacific Ocean

N. V. Zilberman[1] [iD], **D. H. Roemmich**[1] [iD], **and S. T. Gille**[1] [iD]

[1]Scripps Institution of Oceanography, University of California, San Diego, La Jolla, California, USA

Abstract Observations of absolute velocity based on Argo float profiles and trajectories in the ocean interior show evidence for an equatorward current, the East Pacific Rise current, between 42°S and 30°S, along the western flank of the East Pacific Rise. The East Pacific Rise current carries predominantly intermediate water masses, including Subantarctic Mode Water and Antarctic Intermediate Water, and deeper waters, from the southern edge of the subtropical gyre toward the Equator. The 2004 to 2014 mean East Pacific Rise current transport extrapolated through the 0–2600 m depth range is 8.1 $\pm$ 1.6 sverdrup (Sv) (1 Sv = 10^6 m^3 s^{-1}), consistent with a wind-driven interior transport influenced by the East Pacific Rise topography. While deep ocean mixing and geothermal heating can both create pressure gradients that support geostrophic flows in the deep ocean, this study indicates that about half of the East Pacific Rise current transport is associated with topographic steering of the deep flow over the East Pacific Rise.

1. Introduction

The meridional pathways that connect high latitudes to low latitudes are important elements in the ocean's Meridional Overturning Circulation and play a critical role in redistributing heat and freshwater throughout the global ocean [*Trenberth et al.*, 2009]. Within the subtropical gyres, the poleward flow in western boundary currents tends to be balanced by equatorward flow in the ocean interior. Intermediate water masses play a fundamental role in the oceanic heat and freshwater uptake in the Southern Ocean [*Naveira Garabato et al.*, 2009], and they are key indicators of climate change [*Banks and Bindoff*, 2003]. In this study, we address the question of whether the meridional transports that carry intermediate water masses in the South Pacific subtropical gyre interior are influenced by topographic steering over the East Pacific Rise (EPR).

Sverdrup [1947] laid the foundations for studying large-scale wind-driven circulation in the ocean interiors. The basic Sverdrup balance, for a flat-bottomed ocean, accounts for meridional transport in a substantial fraction of the oceans [*Wunsch*, 2011; *Gray and Riser*, 2014] while assuming that both the wind-driven meridional and vertical velocities are negligibly small at a depth above the abyssal flow. This flat-bottomed condition does not hold where wind-driven upper ocean flow is steered by mid-ocean ridges [*Hughes*, 2005]. Although the steering effect of mid-ocean ridges on the ocean circulation is known from theory [e.g., *Marshall*, 1995], it has not been directly tested with observations of absolute geostrophic transport. Historically, studies of deep-ocean transport over the EPR topography have focused on flow associated with geothermal heating and mixing [e.g., *Hautala and Riser*, 1993; *Thurnherr et al.*, 2011].

Because ship-based velocity measurements and current meter data are concentrated near continents, until recently accurate measures of volume transport in the ocean interior were difficult to obtain. With the historical temperature and salinity profiles, the challenge has been to estimate velocities at the reference level [e.g., *Wunsch*, 1996]. Earlier estimates of volume transport in the subtropical South Pacific gyre interior are based on sparse one-time hydrographic and current measurements, including World Ocean Circulation Experiment float observations and moored arrays in confined areas [e.g., *Wijffels et al.*, 2001; *Macdonald et al.*, 2009]. The full development of the global array of autonomous profiling Argo floats has transformed the study of the large-scale circulation of the ocean. Argo floats provide estimates of the shear between 2000 m and the ocean surface, and their trajectories at 1000 m provide a reference velocity. Recent efforts have improved the quality and accessibility of Argo trajectory data [*Ollitrault and Rannou*, 2013].

Argo-based estimates of the geostrophic transport at 32°S from *Zilberman et al.* [2014, Figure 5] showed that, in the interior of the South Pacific subtropical gyre east of the dateline, 41% of the total volume transport in the top 2000 m, a total of 11.4 sverdrup (Sv) of northward transport, was concentrated over the EPR. Analysis of

historical data [*Reid*, 1997] indicated that portions of the South Pacific subtropical gyre extend below 3000 m and are split by the topography along the EPR. Results from *Gray and Riser* [2014, 2015] suggested that the geostrophic transport at middepth is influenced by topographic forcing over mid-ocean ridges. This paper extends *Zilberman et al.*'s [2014] and *Gray and Riser*'s [2014] work, using Argo trajectory data together with density-derived shear, to provide assessments of the meridional transport associated with deep flow steering over the EPR topography. We show evidence for a broad maximum in the northward velocity, which extends up through the water column, on the west side of the EPR between 30°S and 42°S. The enhanced northward flow is here termed the East Pacific Rise current. Results from the present work indicate that half of the East Pacific Rise current transport is generated by deep flow steering over topography.

2. Method

2.1. Argo-Based Geostrophic Transport

Temperature and salinity fields can be used to calculate density, which via the geostrophic relationship allows the ocean velocity and transport to be determined relative to a reference level [*Gill*, 1982, pp. 215–216]. For this study, quality-controlled Argo temperature and salinity profiles [*Roemmich and Gilson*, 2009] are combined with trajectory-based reference velocities at 1000 m to estimate total geostrophic velocities. The time period extends from 2004–2014. The study region (42°S to 30°S and 124°W to 100°W) extends from a northern boundary located south of the Easter Fracture Zone (dashed blue line) to a southern boundary at the poleward limb of the subtropical gyre (Figure 1). During 2004–2014, about 97% of the Argo profiles gathered in this region extended to 1800 m depth. To provide maximal spatial coverage, we focus on the data recorded within 0–1800 m.

To minimize errors in volume transport generated from heterogeneous Argo sampling over the EPR, temperature, salinity, and trajectory-based velocities are grouped into bins. Each bin is elongated in the north-south direction to preserve zonal pressure gradients associated with meridional flow over the Ridge. Following *Zilberman et al.* [2014], temperature, salinity, and trajectory-based velocities are grouped and averaged over 3° latitude × 1/2° longitude north-south oriented bins. In our study region, the number of profiles per 3° latitude × 1/2° longitude bin ranges from 10 to 100, with an average of 40 profiles per bin (Figure S1 in the supporting information). A total of 74 floats are used for the present calculations, all transmitting via Service Argos. About 99% of the float cycles have at least six position fixes at the surface. For these floats, the float drift at parking depth is computed using surfacing and diving positions extrapolated from position fixes at surfacing and diving time following *Park et al.*'s [2009] method. For the remaining 1% of float cycles, the float drift at 1000 m is estimated from the first and last position fixes at the surface. Only Argo floats programmed to park at 1000 dbar were considered for this analysis. Parking pressures, for all cycles considered here, vary between 910–1130 dbar. Using the mean shear between 1000 m and the parking depth would lead to small ($< 2 \times 10^{-4}$ m s^{-1}) changes in horizontal velocity at 1000 m.

Shear-induced error (E_{Sys}) is caused by the vertical shear in horizontal velocity, displacing the float during its rise and fall between the sea surface and 2000 m profile depth. Here E_{Sys} is computed assuming that the float spends 5% of the cycle time rising and descending between the sea surface and the 1000 m parking depth. A correction is made by adjusting the mean volume transport to remove E_{Sys}. Uncertainties in volume transport estimates (E_R) are computed using standard error based on variability in trajectory-based velocity at 1000 m and trajectory density per 3° latitude × 1/2° longitude bin. Estimates of meridional geostrophic velocity from a 2010 hydrographic cruise (data archived by the National Oceanographic Data Center), at 32.5°S, and averaged between 117°W and 108°W, yield a small deviation from an assumption of constant vertical shear below 1800 m depth, equal to that in the 1600–1800 m range (Figure S2), which when integrated vertically and zonally would lead to a 0.23 Sv difference in the volume transport. Horizontal velocities and volume transport are extrapolated linearly from 1800 m to a nominal maximum depth at the ridge crest of 2600 m from a fit to the shear between 1600 m and 1800 m depth with the assumption that depth variations in the vertical shear between 1800 m depth and the bottom are small over the EPR. The geostrophic transport between 2600 m and the bottom slope of the EPR is not considered in this study and does not impact Subantarctic Mode Water (SAMW) and Antarctic Intermediate Water (AAIW) transport estimates. Pressure fields are computed using the objective mapping algorithm described by *Bretherton et al.* [1976] and *Gille* [2003]. A Gaussian decorrelation with an e-folding scale of 3° in latitude and 0.5° in longitude function is used for the objective mapping algorithm. Pressure field estimates, computed using isotropic e-folding scale of 2° × 2° , showed similar large-scale structures (not shown).
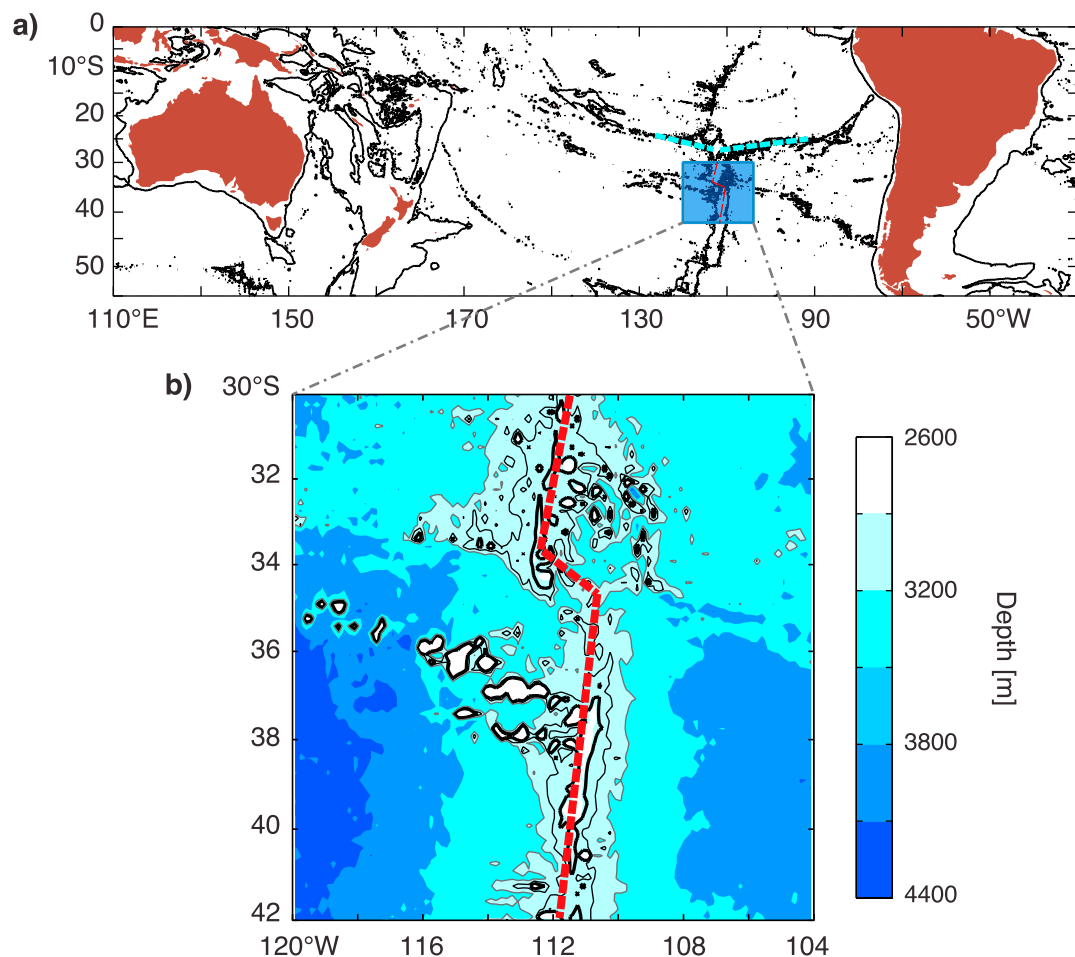
Figure 1. (a) The dark blue boxed region, 42°S to 30°S, 120°W to 104°W, indicates the location of the study area in the South Pacific Ocean. The black contours indicate 3000 m depth. The dashed red line indicates the EPR. The dashed blue line indicates the Easter Fracture Zone. (b) ETOPO2 2 min bathymetry over the EPR. The contour lines indicate 2600 m (thickest black), 2800 m (thin black), and 3000 m (thin gray) depth. The crest of the EPR is indicated in red.

2.2. Geostrophic Transport Estimated From Wind Forcing

The zonally integrated meridional component of the geostrophic transport estimated from wind forcing is described in the Sverdrup relation

$$(V_g)_{wind} = V_{Sv} - V_{Ek} \tag{1}$$

$$= \int \left[\left(\frac{1}{\rho_0 \beta} \mathbf{k} \cdot \mathbf{\nabla} \times \tau \right) - \left(\frac{-\tau^x}{\rho_0 f} \right) \right] dx,$$

where the first term on the right-hand side of equation (1) is the Sverdrup transport and the second term is the Ekman transport [*Gray and Riser*, 2014]. The term *V* indicates the zonally and vertically integrated transport. In equation (1), *x* is the longitude, ρ_0 is the reference density, *f* is the Coriolis parameter, $\beta = df/dy$ is the meridional gradient of the Coriolis parameter, *y* is the latitude, **k** is the unit vector in the vertical direction, and $\tau = (\tau^x, \tau^y)$ is the wind stress vector averaged between 2004 and 2014. The average surface stress is computed from the monthly means of daily mean fields in the Re-Analysis (ERA)/Interim archive available on the European Centre for Medium-Range Weather Forecasts (ECMWF) Web site (http://data-portal.ecmwf.int/) [*Berrisford et al.*, 2009] and from monthly means of 6-hourly fields in the National Centers for Environmental Prediction (NCEP) / National Center for Atmospheric Research archive available from the NCEP Web site (http://www.esrl.noaa.gov) [*Kalnay et al.*, 1996]. Geostrophic transport estimates from wind forcing computed between 42°S and 30°S using ECMWF are not significantly different from those using NCEP (not shown) based on the standard error of 1 year mean transport anomalies. The $(V_g)_{wind}$ estimates presented in section 3 are computed using ECMWF.

2.3. Geostrophic Transport Enhancement Estimated From Topographic Steering

The meridional component of the vertically and zonally integrated geostrophic transport, estimated from deep-flow steering over topography, is

$$(V_g)_{topo} = -\int \frac{f}{\beta} w_B dx \tag{2}$$

$$= \int \frac{f}{\beta} \left(u_B \frac{\partial H}{\partial x} + v_B \frac{\partial H}{\partial y} \right) dx,$$

where H is the bottom depth, w_B is the vertical velocity at the bottom, and (u_B, v_B) are the zonal and meridional components of the velocity vector at the bottom [*Jackson et al.*, 2006]. $(V_g)_{topo}$ estimates are calculated for 0–2600 m, assuming a constant vertical shear below 1800 m depth, equal to that in the 1600–1800 m depth range. Values of (u_B, v_B), estimated at 2600 m (see section 2.1), and H, taken from the ETOPO2 dataset [*Smith and Sandwell*, 1997], are smoothed using an 8° latitude × 8° longitude running mean.

For 37–30°S, $(V_g)_{topo}$ is generated mostly by the large-scale crest of the EPR shoaling northward ($\frac{\partial H}{\partial y} < 0$) and the ridge widening northward (Figure S3). Between 42°S and 37°S, the large-scale depth of the EPR shows limited changes with latitude. In contrast, the depth of the EPR varies in the zonal direction and is characterized by a more abrupt slope on the western side of the ridge than on the eastern side. For this latitude range, $(V_g)_{topo}$ is mainly associated with the large-scale slope of the EPR shoaling eastward ($\frac{\partial H}{\partial x} < 0$). Our measurements imply vertical velocity at 2600 m, averaged over 117–108°W longitude, in the 0.2–2.4×10^{-6} m s^{-1} range between 30° and 42°S (Figure S4). The vertical velocity estimate averaged over 117°–108°W and 30°–42°S is $1.2 \times 10^{-6} \pm 0.3 \times 10^{-6}$ m s^{-1}, of the same order (but opposite sign) as Ekman pumping in the same region (not shown). Error bars in w_B and $(V_g)_{topo}$ are computed using the standard error of the velocity field at 2600 m in equation (2) based on variability in trajectory-based velocity at 1000 m and Argo sampling density per 3° latitude × 1/2° longitude bin. An additional source of uncertainty in $(V_g)_{topo}$ is introduced by the assumption of constant vertical shear below 1800 m. Alternative means of estimating the velocity shear near the ocean bottom include assuming no shear between 1800 m and 2600 m. Using this method leads to $(V_g)_{topo}$ estimates across 117–108°W, averaged over 30°–42°S latitude range, which are 45% (2.4 ± 1.1 Sv) lower than estimates using constant shear below 1800 m (not shown). Extrapolating horizontal velocities to 2900 m, the averaged bottom depth between 117–108°W and 42–30°S, would not lead to significant changes in our estimate of the vertical velocity at the bottom.

2.4. Topographic Sverdrup Transport

In the case of a wind-driven gyre extending to the ocean bottom and/or interacting with deeper flow that extends upward from the topography along the EPR, if the advection terms in the vorticity balance are neglected, the meridional transport over the EPR can be inferred directly from the sum of the transports associated with topographic steering, $(V_g)_{topo}$, and wind forcing, $(V_g)_{wind}$ (see sections 2.2–2.3), using the modified expression of the basic Sverdrup balance [e.g., *Marshall*, 1995]

$$(V_g)_{tot} = (V_g)_{wind} + (V_g)_{topo} \tag{3}$$

$$= \int \left[\left(\frac{1}{\rho_0 \beta} \mathbf{k} \cdot \nabla \times \boldsymbol{\tau} \right) - \left(\frac{-\tau^x}{\rho_0 f} \right) - \frac{f}{\beta} w_B \right] dx$$

Estimates of the topographic Sverdrup transport, $(V_g)_{tot}$, will be compared to transport estimates calculated directly from Argo data, V, to determine how important topographic influence is over the EPR.

3. Results

Maps of the geostrophic pressure field at 1000 m (Figure 2) indicate the direction and strength of the geostrophic flow at that depth [*Davis*, 1998]. Flows are cyclonic (clockwise in the Southern Hemisphere) around low pressure centers. For this study, the pressure field is estimated in two different ways from Argo data collected between 2004 and 2014. Figure 2a shows the pressure field calculated from Argo trajectories at 1000 m (trajectory-based calculation), and Figure 2b shows the pressure field at 1000 m calculated from Argo temperature and salinity profiles through the thermal wind relationship, referenced to 1800 m (reference-level calculation). The fields are computed using consistent horizontal resolution (see section 2.1). Nonetheless, the two pressure fields differ substantially. In the trajectory-based calculation, the large high-pressure anomaly on
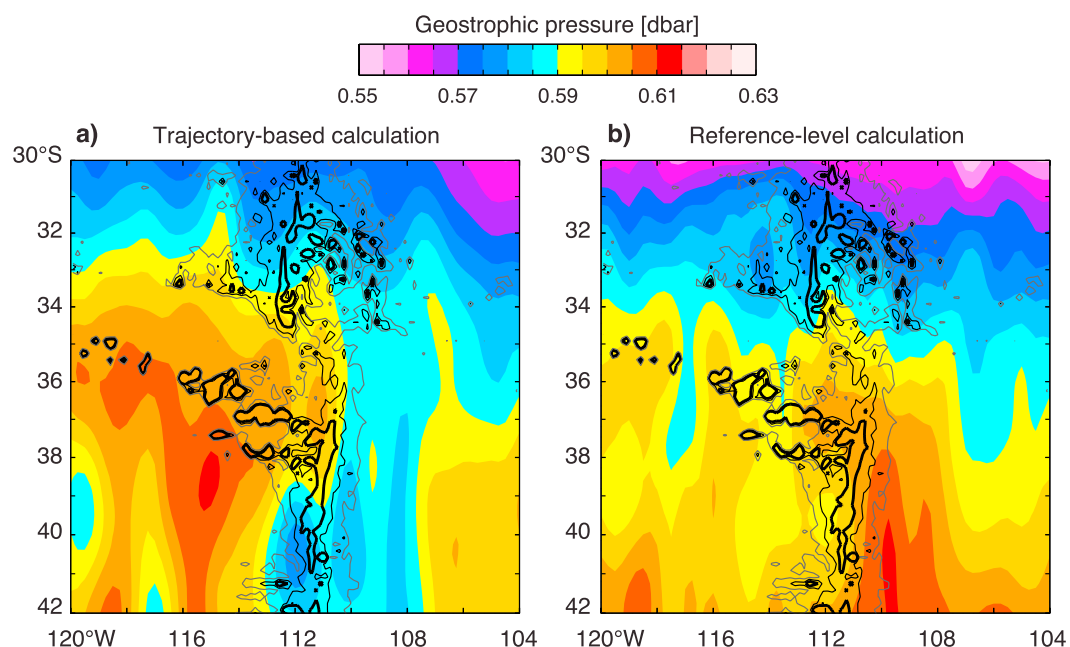
Figure 2. Geostrophic pressure field at 1000 m computed using (a) trajectory-based velocities and (b) a reference level at 1800 m. The contour lines indicate 2600 m (thickest black), 2800 m (thin black), and 3000 m (thin gray) depth.

the western flank of the EPR shows a dominant northward flow between 42°S and 30°S (Figure 2a). In contrast, high-pressure anomalies that spread across the study region in the reference-level calculation are indicative of a nearly zonal west-northwest flow between 35°S and 30°S (Figure 2b). South of 35°S the pressure field in the reference-level calculation indicates a southward flow, opposite in direction to the trajectory-based calculation (Figure 2).

The meridional velocities associated with the pressure fields shown in Figure 2 are zonally integrated to give the meridional transport (per unit depth) at 1000 m (Figure 3a). Averaged between 30°S and 42°S, the trajectory-based and reference-level calculations both indicate modest meridional transport at 1000 m west of 117°W and slowly increasing transport east of 108°W (Figure 3a). Over the EPR, the trajectory-based transport at 1000 m diverges from the reference-level estimate, as shown in Figure 3a. In the trajectory-based calculation, the meridional transport per unit depth is 2756 $m^2 s^{-1}$ greater at 108°W than at 117°W, equivalent to a velocity difference of 0.3 cm s^{-1} over a width of 835 km. In contrast, there are no significant spatial differences in meridional transport in the reference-level calculation for this longitude range.

The enhanced northward flow estimated in the trajectory-based calculation extends up through the water column. Because its path follows the ocean bottom topography, we call it the East Pacific Rise current. Figure 3b shows a zonal section of the meridional geostrophic velocity, based on geostrophic shear and trajectory-derived reference velocities, averaged between 30°S and 42°S. The geostrophic velocities are smoothed using a 6° longitude running mean for display purposes only. Northward flow is positive. Between 117°W and 108°W, elevated (> 0.2 cm s^{-1}) northward velocities extend between the sea surface and 1800 m. Below 1000 m depth, velocities on the western flank of the EPR are higher than to the west, and they are opposite in direction and stronger than the flow east of the ridge. Figure 3c shows the depth distribution of the time-mean geostrophic transport integrated across the flanks of the EPR between 117°W and 108°W, averaged over the 30°–42°S latitude range. The trajectory-based transport estimate is northward at all depths (see section 2.1 for details of calculation and uncertainties). In contrast, the transport in the 1800 m reference-level calculation is southward below 900 m (Figure 3c). The statistically significant northward transport between 1300 and 1800 m in the trajectory-based calculation demonstrates that the subtropical gyre extends to at least 1800 m depth and/or interacts with deeper flow that is moving over the bottom slope on the flanks of the EPR. Discrepancies between the depth distribution of Argo-based (Figure 3c) and ship-based (Figure S2) transport estimates are attributed to differences in the time period and latitude considered for the two data sources.
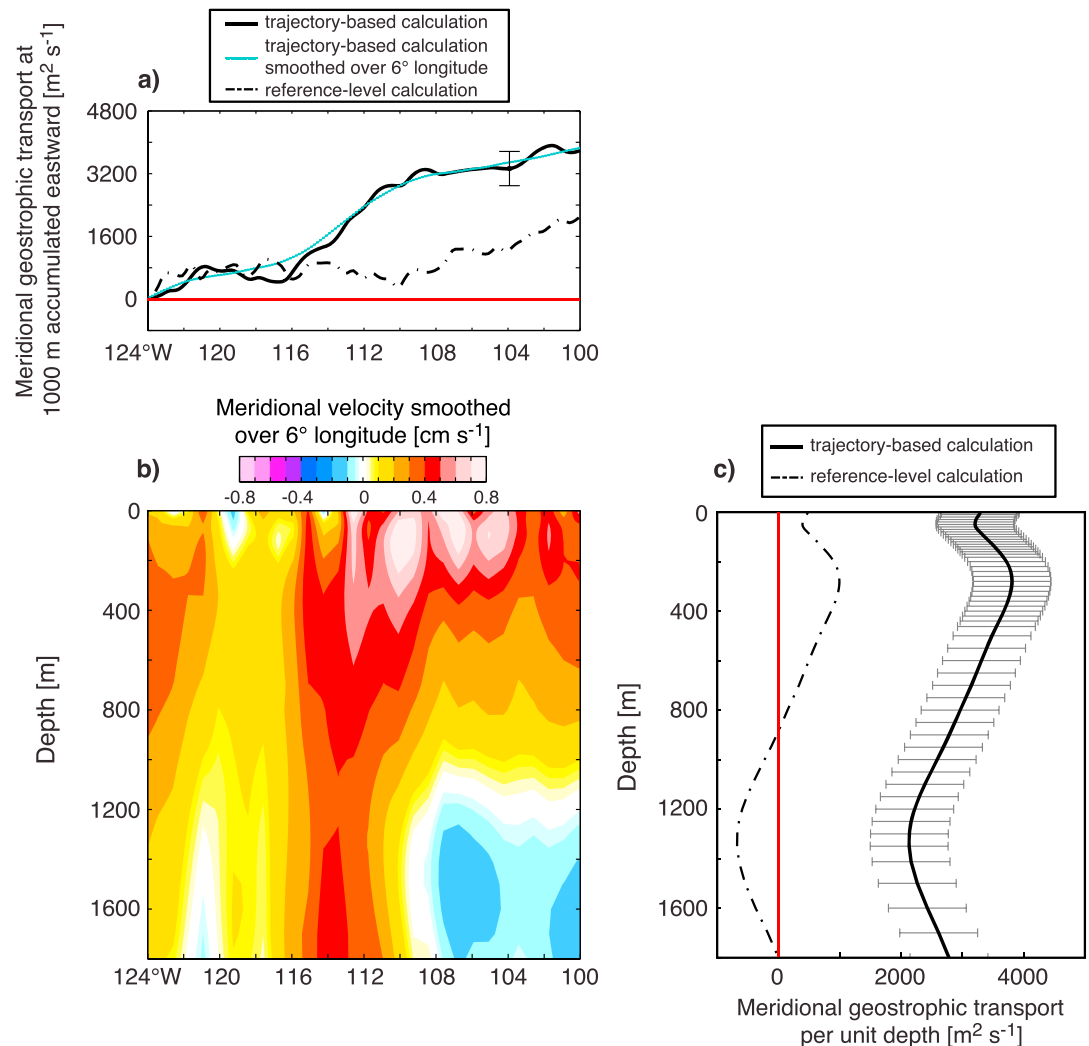
Figure 3. (a) Geostrophic transport at 1000 m averaged between 30°S and 42°S accumulated from 124°W eastward based on trajectories (solid black) and relative to 1800 m (dashed black). The error bar in black shows random error generated from heterogeneous trajectory density. The blue line shows geostrophic transport accumulated eastward based on geostrophic velocities smoothed using a 6° longitude running mean. (b) Meridional geostrophic velocity, based on geostrophic shear and trajectory-derived reference velocities, averaged between 30°S and 42°S. The geostrophic velocities are smoothed using a 6° longitude running mean for display purposes only. (c) Estimate of the meridional geostrophic transport per unit depth, computed using trajectory-based reference velocity with a correction for shear-induced error (E_{Sys}), averaged between 30°S and 42°S, and integrated between 117°W and 108°W (solid black), and meridional geostrophic transport per unit depth relative to 1800 m (dashed black). The error bars in gray color show random errors generated from heterogeneous trajectory density.

Transport estimates across 117–108°W calculated from wind forcing and topographic steering (equations (1)–(3)) and estimated using trajectory-based velocities are shown in Figure 4. The Sverdrup relation predicts a nearly constant zonally integrated meridional transport estimated from wind forcing without topographic enhancement between 42°S and 30°S (solid magenta line), substantially smaller than in the trajectory-based calculation for 0–1800 m (solid green line with gray error). The largest differences between the Sverdrup relation and trajectory-based estimates are between 32.5°S and 30°S, in the latitude band considered by *Zilberman et al.* [2014], and between 38°S and 35°S (Figure 4). Between 42°S and 30°S, the averaged 0–1800 m trajectory-based transport is 5.1 ± 1.1 Sv (1 Sv = 10^6 m^3 s^{-1}), compared to 2.9 Sv predicted by the simple Sverdrup relation. The trajectory-based calculation indicates a northward transport of 4.3 ± 0.9 Sv of water masses below potential density (σ_θ) 26.5 kg m^{-3}, including 1.3 ± 0.2 Sv of SAMW between $\sigma_\theta = 26.5$ kg m^{-3} and $\sigma_\theta = 27$ kg m^{-3} [*McCartney*, 1977; *Hanawa and Talley*, 2001], 1.5±0.3 Sv of AAIW between $\sigma_\theta = 27$ kg m^{-3} and $\sigma_\theta = 27.3$ kg m^{-3} [*Emery*, 2001], and 1.5 ± 0.4 Sv of Pacific Deep Water below
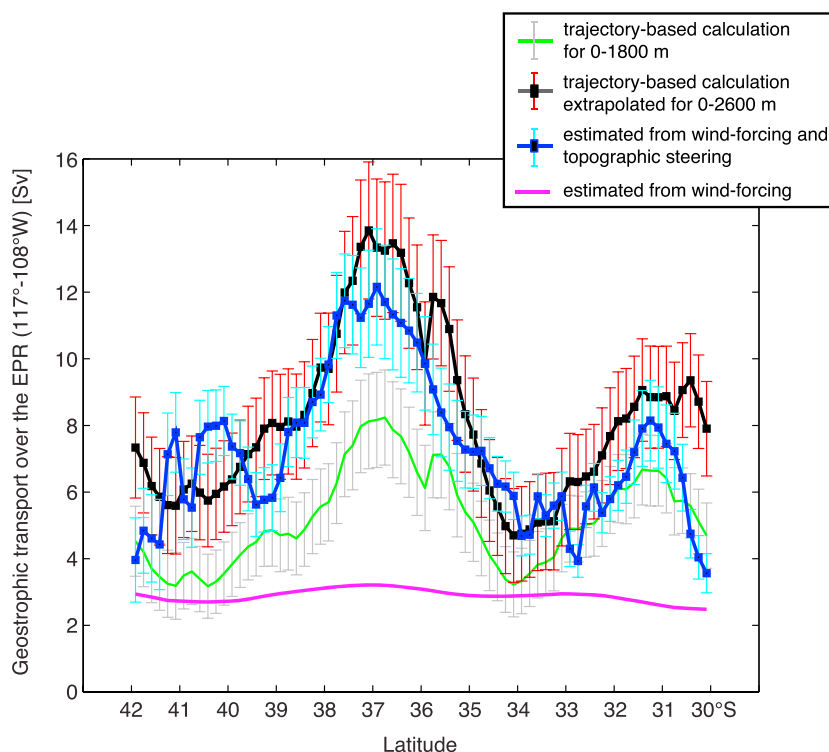
Figure 4. Trajectory-based meridional geostrophic transports are integrated for 0–1800 m (solid green line with gray error bars) and 0–2600 m (solid black line with red error bars, *V*) between 117°W and 108°W. The error bars show random error generated from heterogeneous trajectory density. The sum of volume transports estimated from wind forcing and topographic steering, $(V_g)_{tot}$, is shown in blue. The error bars in light blue show random errors of $(V_g)_{topo}$ associated with the velocity field at 2600 m depth. Meridional volume transport estimated from wind forcing, $(V_g)_{wind}$, is shown in magenta.

$\sigma_\theta = 27.3$ kg m^{-3} [*Talley*, 2003]. Based on Chlorofluorocarbon (CFC)-derived formation rates [*Hartin et al.*, 2011], the enhanced northward flow over the EPR contributes 18% of the SAMW and 26% of the AAIW transport in the South Pacific subtropical gyre interior.

The striking presence of northward velocities along the western flank of the EPR in the trajectory-based estimates indicates that topography plays a role in controlling transport. The 42°S–31°S average trajectory-based transport estimate for 0–2600 m across 117–108°W, of 8.1 ± 1.6 Sv, agrees within error with the topographic Sverdrup transport, of 7.4 ± 1.1 Sv, of which 61% is associated with topographic steering and 39% is generated by wind forcing. Between 31°S and 30°S, $(V_g)_{tot}$ estimates across 117–108°W (blue line) are significantly smaller than trajectory-based transports (black line, *V*). Differences between $(V_g)_{tot}$ and *V* could result from (i) additional flow generated by geothermal heating and vertical mixing, (ii) depth-dependent shear below 1800 m, (iii) advective terms in the vorticity balance, and (iv) shear between 2600 m and the bottom slope on the flanks of the EPR.

Observational studies, north of our study region, suggest that vertical mixing and geothermal heating over the EPR generate anticyclonic flow near the ocean bottom [*Hautala and Riser*, 1993; *Thurnherr et al.*, 2011]. *Thurnherr et al.* [2011] describe an anticyclonic gyre driven by geothermal heating centered on the crest of the EPR at 9°–10°N, with associated southward flow on the western flank of the ridge, and northward flow on the eastern flank. *Hautala and Riser* [1993] document an anticyclonic circulation generated by vertical mixing centered to the west of the EPR at 25°–5°S, which generates northward transport on the western flank, near the crest of the ridge, and southward transport 1000–2000 km to the west. Measurements of the absolute geostrophic flow described here show a substantial enhancement of meridional transport over the EPR, compared with either transport referenced to 1800 m, transport estimated from wind stress curl, or estimates remote from the ridge, farther east or west. The spatial distribution of the flow enhancement over the EPR is consistent with flow along the sloping bottom generated by linear vorticity dynamics. Because our transport

estimates are integrated over a broad region centered on the ridge's crest, geothermal heating along the ridge crest should have a small impact on the meridional transport over the EPR. Opposing flows on opposite flanks of the EPR are expected to have canceling effects [*Thurnherr et al.*, 2011]. Pressure anomalies associated with vertical mixing that is displaced from the ridge crest could lead to geostrophic northward transport on the western flank of the ridge and may explain observed discrepancies between the topographic Sverdrup transport, $(V_g)_{tot}$, and geostrophic transport estimates from the Argo observations, V. An analysis of the integrated effect of (i)–(iv) on the transport over the EPR is beyond the scope of this work.

4. Conclusion

This work has shown a substantial current flowing northward between 30°S and 42°S on the western flank of the EPR, in the South Pacific subtropical gyre interior. The East Pacific Rise current extends between the crest of the EPR and the ocean surface and carries mostly intermediate and deep water masses. Results indicate that the EPR creates a window for the enhanced transport of intermediate waters, from the southern edge of the subtropical gyre toward the tropics, thus providing a pathway for one branch of the Southern Hemisphere Meridional Overturning Circulation.

The present study is the first to test directly the topographic Sverdrup balance with observations of absolute geostrophic transport. The sharp enhancement in the meridional transport over the EPR is a robust feature that departs from conventional assumptions of a simple relationship between wind stress and meridional transport. In the South Pacific subtropical gyre interior between 2600 m depth and the ocean surface, about half of the enhanced volume transport seen over the EPR can be explained by topographic steering over the ridge topography. The transport strengthening seen in the South Pacific subtropical gyre interior occurs because the wind-driven circulation extends deeper than the top of the EPR and/or interacts with deeper flow that extends upward from the ridge topography. Results from our analysis have implications beyond the South Pacific Ocean, since there are other mid-ocean ridges that extend upward into the depth range of the gyre interior circulations. This suggests that other pathways along mid-ocean ridges in the North Pacific, Atlantic and Indian Oceans may play similar roles. The new understanding that emerges from this study has the potential not just to redraw our map of ocean currents but also to improve estimates of global ocean mass, heat, and freshwater transports that are critical for projecting the ocean's contributions to climate change.

Argo trajectory-based reference velocities, combined with geostrophic shear, are essential to obtain accurate measures of upper-ocean volume transport. Conventional Argo floats over the EPR have obtained profiles to 2000 m or less, and ship-based measurements in this region are too sparse in time to provide a representative estimate of the mean deep transport near topography. Uncertainties in studies of the mid-ocean ridge's influence on the volume transport in the subtropical gyre interiors will be substantially reduced by measuring ocean geostrophic velocities to the seafloor. The development and testing of deep Argo floats, capable of diving to the ocean bottom (6000 m depth), is underway to improve the sampling of the deep ocean.

References

Berrisford, P., D. Dee, K. Fielding, M. Fuentes, P. Kallberg, S. Kobayashi, and S. Uppala (2009), The ERA-Interim archive, version 1.0, *Tech. Rep. ERA Rep. Ser. 1*, 16 pp., European Centre for Medium Range Weather Forecasts, Shinfield Park, Reading, U. K.

Banks, H., and N. L. Bindoff (2003), Comparison of observed temperature and salinity changes in the Indo-Pacific with results from the coupled climate model HadCM3: Processes and mechanisms, *J. Climate, 16*, 156–166.

Bretherton, F. P., R. E. Davis, and C. B. Fandry (1976), A technique for objective analysis and design of oceanographic experiments applied to MODE—73, *Deep-Sea Res., 23*, 559–582.

Davis, R. E. (1998), Preliminary results from directly measuring middepth circulation in the tropical and South Pacific, *J. Geophys. Res., 103*(C11), 24,619–24,639.

Emery, W. J. (2001), Water types and water masses, in *Encyclopedia of Ocean Sciences*, edited by J. Steele, S. Thorpe, and K. Turekian, pp. 3179–3187, Acad. Press, Cambridge, Mass.

Naveira Garabato, A. C., L. Jullion, D. P. Stevens, K. K. Heywood, and B. A. King (2009), Variability of Subantarctic Mode Water and Antarctic Intermediate Water in the Drake Passage during the late-twentieth and early-twenty-first centuries, *J. Climate, 22*, 3661–3688.

Gill, A. E. (1982), *Atmosphere-Ocean Dynamics*, 662 pp., Acad. Press, New York.

Gille, S. T. (2003), Float observations of the Southern Ocean Part I: Estimating mean fields, bottom velocities, and topographic steering, *J. Phys. Oceanogr., 33*, 1167–1181.

Gray, A. R., and S. C. Riser (2014), A global analysis of Sverdrup balance using absolute geostrophic velocities from Argo, *J. Phys. Oceanogr., 44*, 1213–1229.

Gray, A. R., and S. C. Riser (2015), Reply to "Comments on 'A global analysis of Sverdrup balance using absolute geostrophic velocities from Argo' ", *J. Phys. Oceanogr., 45*, 1449–1450.

Hanawa, K., and L. D. Talley (2001), *Ocean Circulation and Climate*, 373–386 pp., Acad. Press, Cambridge, Mass.

Hartin, C. A., R. A. Fine, B. M. Sloyan, L. D. Talley, T. K. Chereskin, and J. Happel (2011), Formation rates of Subantarctic mode water and Antarctic intermediate water within the South Pacific, *Deep-Sea Res. I, 58*, 524–534.

Hautala, S. L., and S. C. Riser (1993), A nonconservative β-spiral determination of the deep circulation in the Eastern South Pacific, *J. Phys. Oceanogr.*, *23*, 1975–2000.

Hughes, C. W. (2005), Nonlinear vorticity balance of the Antarctic Circumpolar Current, *J. Geophys. Res.*, *110*, C11008, doi:10.1029/2004JC002,753.

Jackson, L., C. W. Hughes, and R. G. Williams (2006), Topographic control of basin and channel flows: The role of bottom pressure torques and friction, *J. Phys. Oceanogr.*, *36*.

Kalnay, E., et al. (1996), The NCEP/NCAR 40-year reanalysis project, *Bull. Am. Meteorol. Soc.*, *77*, 437–471.

Macdonald, A. M., S. Mecking, P. E. Robbins, J. M. Toole, G. C. Johnson, L. Talley, M. Cook, and S. E. Wijffels (2009), The WOCE-era 3-D Pacific Ocean circulation and heat budget, *Prog. Oceanogr.*, *82*, 281–325.

Marshall, D. P. (1995), Influence of topography on the large-scale ocean circulation, *J. Phys. Oceanogr.*, *25*, 1622–1635.

McCartney, M. S (1977), A voyage of discovery, *Deep-Sea Res.*, 103–119.

Ollitrault, M., and J. P. Rannou (2013), ANDRO: An Argo-based deep displacement dataset, *J. Atmos. Oceanic Technol.*, *30*, 759–788.

Park, J., K. Kim, B. King, and S. Riser (2009), An advanced method to estimate deep currents from profiling floats, *J. Atmos. Oceanic Technol.*, *22*, 1294–1304.

Reid, J. L. (1997), On the total geostrophic circulation of the Pacific Ocean: Flow patterns, tracers, and transports, *Prog. Oceanogr.*, *39*, 263–352.

Roemmich, D. H., and J. Gilson (2009), The 2004–2008 mean and annual cycle of temperature, salinity, and steric height in the global ocean from Argo Program, *Prog. Oceanogr.*, *82*, 81–100.

Smith, W. H. F., and D. T. Sandwell (1997), Global seafloor topography from satellite altimetry and ship depth soundings, *Science*, *277*, 1957–1962.

Sverdrup, H. (1947), Wind-driven currents in a baroclinic ocean; with application to the equatorial currents of the eastern Pacific, *Proc. Natl. Acad. Sci. U.S.A.*, *33*(11), 318–326.

Talley, L. D. (2003), Shallow, intermediate, and deep overturning components of the global heat budget, *J. Phys. Oceanogr.*, *33*, 530–560.

Thurnherr, A. M., J. R. Ledwell, J. W. Lavelle, and L. S. Mullineaux (2011), Hydrography and circulation near the crest of the East Pacific Rise between 9° and 10°N, *Deep-Sea Res.*, *58*, 365–376.

Trenberth, K. E., J. T. Fasullo, and J. Kiehl (2009), Earth's global energy budget, *Proc. Natl. Acad. Sci. U.S.A.*, *90*, 311–323.

Wijffels, S. E., J. M. Toole, and R. Davis (2001), Revisiting the South Pacific subtropical circulation: A synthesis of World Ocean Circulation Experiment observations along 32°S, *J. Geophys. Res.*, *106*(C9), 19,481–19,513.

Wunsch, C. (1996), *The Ocean Circulation Inverse Problem*, Cambridge Univ. Press, Cambridge, U. K.

Wunsch, C. (2011), The decadal mean ocean circulation and Sverdrup balance, *J. Mar. Res.*, *69*, 417–434.

Zilberman, N. V., D. H. Roemmich, and S. T. Gille (2014), Meridional volume transport in the South Pacific: Mean and SAM-related variability, *J. Geophys. Res.*, *119*(4), doi:10.1002/2013JC009,688.